

A novel assessment of whole-mount Gleason grading in prostate cancer to identify candidates for radical prostatectomy: a machine learning-based multiomics study

Jing Ning^{*1,2,3}, Clemens P. Spielvogel^{*1,3}, David Haberl^{1,3}, Karolina Tractova^{1,4}, Stefan Stoiber^{1,2}, Sazan Rasul³, Vojtech Bystry⁴, Gabriel Wasinger², Pascal Baltzer⁵, Elisabeth Gurnhofer², Gerald Timelthaler⁶, Michaela Schleederer², Laszlo Papp⁷, Helga Schachner², Thomas Helbich⁵, Markus Hartenbach³, Bernhard Grubmüller^{8,9}, Shahrokh F Shariat^{8,10,11,12,13,14}, Marcus Hacker³, Alexander Haug^{1,3}, Lukas Kenner^{1,2,15,16,17}

*First authors contributed equally

Running title: Next-Gen Prostatectomy: ML-Driven whole-mount Gleason Grading

¹ Christian Doppler Laboratory for Applied Metabolomics, 1090 Vienna, Austria.

² Clinical Institute of Pathology, Department for Experimental and Laboratory Animal Pathology, Medical University of Vienna, Vienna, Austria

³ Division of Nuclear Medicine, Department of Biomedical Imaging and Image-Guided Therapy, Medical University of Vienna, 1090 Vienna, Austria.

⁴ Central European Institute of Technology, Masaryk University, Brno 62500, Czech Republic.

⁵ Department of Biomedical Imaging and Image-guided Therapy, Division of Molecular and Gender Imaging, Medical University of Vienna, 1090 Vienna, Austria.

⁶ Center for Cancer Research, Medical University of Vienna, 1090 Vienna, Austria.

⁷ Center for Medical Physics and Biomedical Engineering, Vienna, Austria.

⁸ Department of Urology, Medical University of Vienna, Vienna, Austria.

⁹ Working Group of Diagnostic Imaging in Urology, Austrian Society of Urology, Vienna, Austria.

¹⁰ Karl Landsteiner Institute of Urology and Andrology, Vienna, Austria.

¹¹ Department of Urology, University of Texas Southwestern, Dallas, Texas.

¹² Division of Medical Oncology, Department of Urology, Weill Medical College of Cornell University, New York, New York.

¹³ Department of Urology, Second Faculty of Medicine, Charles University, Prague, Czech Republic.

¹⁴ Institute for Urology and Reproductive Health, I.M. Sechenov First Moscow State Medical University, Moscow, Russia.

¹⁵ Unit of Laboratory Animal Pathology, University of Veterinary Medicine Vienna, 1210 Vienna, Austria.

¹⁶ Comprehensive Cancer Center, Medical University Vienna, Vienna, Austria.

¹⁷ Center for Biomarker Research in Medicine (CBmed), Graz, Styria, Austria

Corresponding author: Lukas Kenner

Address: Währinger Gürtel 18-20 1Q, 1090 Vienna, Austria;

E-mail: lukas.kenner@meduniwien.ac.at;

Tel: +43 1 40400 36590

Author contributions

JN and CPS conceived and conducted the study. JN, CPS, EG, SS and SR participated in gathering and cleaning the raw data. JN, LK and GW performed data annotation. DH, VB, SS and KT were involved in feature extraction from raw data and visualization. EG, GT, MS and HS provided technical support for histological data. JN and CPS conducted the experiment and analysis, developed the associated software and performed the validation. JN and CPS performed the statistical analysis. LK, AH, LP and MH provided either clinical or technical expertise. JN and CPS designed the figures and wrote the manuscript. All authors reviewed the manuscript and provided critical feedback.

Acknowledgements

The financial support by the Austrian Federal Ministry for Digital and Economic Affairs, the National Foundation for Research, Technology and Development, and the Christian Doppler Research Association is gratefully acknowledged. We thank Siemens Healthineers for the financial and scientific support. We would like to thank the Chinese Scholarship Council for the financial support. We thank Central European Institute of Technology for scientific support. We thank Chun Li and Daniel Frigo for their insightful comments and constructive suggestions. We thank Boris Tichý, Leonhard Müllauer, Brigitte Hantusch, Christina Sternberg, Martin Raigel, Josef Yu and David Iommi for their contribution to this study. L.K. acknowledges the support from MicroONE, CBmed GmbH, the Austrian Research Promotion Agency (FFG), the European Union Horizon 2020 Marie Skłodowska-Curie Doctoral Network grants, the Margaretha Hehberger Stiftung and the Vienna Science and Technology Fund (WWTF).

Abstract

Purpose: This study aims to assess whole-mount Gleason grading (GG) in prostate cancer (PCa) accurately using a multiomics machine learning (ML) model and to compare its performance with biopsy-proven GG (bxGG) assessment.

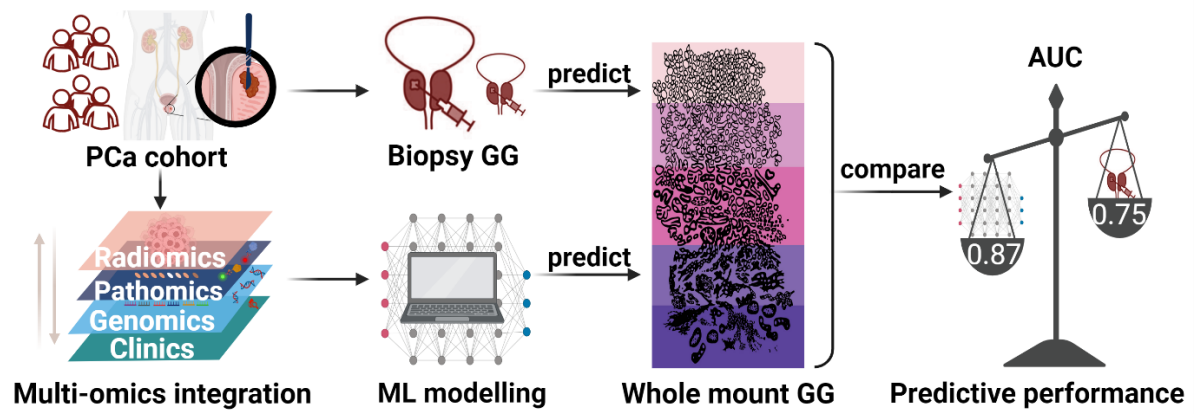
Materials and Methods: A total of 146 patients with PCa recruited in a pilot study of a prospective clinical trial (NCT02659527) were retrospectively included in the side study, all of whom underwent ⁶⁸Ga-PSMA-11 integrated positron emission tomography (PET) / magnetic resonance (MR) before radical prostatectomy (RP) between May 2014 and April 2020. To establish a multiomics ML model, we quantified PET radiomics features, pathway-level genomics features from whole exome sequencing, and pathomics features derived from immunohistochemical staining of 11 biomarkers. Based on the multiomics dataset, five ML models were established and validated using 100-fold Monte Carlo cross-validation.

Results: Among five ML models, the random forest (RF) model performed best in terms of the area under the curve (AUC). Compared to bxGG assessment alone, the RF model was superior in terms of AUC (0.87 vs 0.75), specificity (0.72 vs 0.61), positive predictive value (0.79 vs 0.75), and accuracy (0.78 vs 0.77) and showed slightly decreased sensitivity (0.83 vs 0.89) and negative predictive value (0.80 vs 0.81). Among the feature categories, bxGG was identified as the most important feature, followed by pathomics, clinical, radiomics and genomics features. The three important individual features were bxGG, PSA staining and one intensity-related radiomics feature.

Conclusion: The findings demonstrate a superior assessment of the developed multiomics-based ML model in whole-mount GG compared to the current clinical baseline of bxGG. This enables personalized patient management by identifying high-risk PCa patients for RP.

Keywords: prostate cancer, PSMA, Gleason grading, machine learning, multiomics

Word count: 264/275



Notes: PCa: prostate cancer; ML: machine learning; GG: Gleason grading; AUC: area under the curve.

Introduction

Prostate cancer (PCa) is the second leading cancer-related death in men, with an incidence of nearly 20% worldwide [1]. PCa has the highest five-year survival rate (98%) for all stages combined among different tumor types [2]. As first-line therapy, radical prostatectomy (RP) has substantially contributed to this phenomenon [3]. However, as a consequence of RP, around 31% of patients suffer from urinary incontinence [4], and about 90% suffer from erectile dysfunction [5]. Hence, precise identification of individuals who experience minimal clinical advantages but encounter substantial adverse effects in RP is of utmost importance. Currently, the decision on whether to perform RP is mainly determined by biopsy-proven Gleason score (bxGS)[6]. Despite its important role in identifying PCa type, stage, differentiation, and the resulting influence on treatment modality [7], several studies have revealed a strong discrepancy between bxGS and whole-mount GS after RP[8–10]. Since whole-mount GS holds a strong association with clinical outcomes [11–13], a more reliable method to assess whole-mount Gleason grading (GG) is needed to accurately identify candidates for RP.

Multiomics provides urologists with comprehensive insights into various aspects of PCa [14], including genetic signatures from genomics, molecular heterogeneity from radiomics, and protein expression from pathomics. Genetic tests of PCa biopsy samples are currently available to predict subsequent disease progression after RP [15]. While genomics is nowadays part of the standard repertoire of cancer research approaches, the full prospects of pathomics and positron emission tomography (PET)-based radiomics yet remain to be explored. Radiomics is an emerging field where imaging features are extracted for objective and quantitative tumor characterization[16]. Radiomics application on prostate-specific membrane antigen (PSMA) PET scans has shifted clinical PCa research towards a personalized direction [17,18]. Recent studies have showcased the capability of pathomics, an approach for the extraction of quantitative features from pathological images, in PCa characterization [19–21]. However, no studies have yet leveraged the potential of combining genomics, radiomics, and pathomics. Machine learning (ML) can serve as an ideal platform for the integration of high-dimensional multiomics data.

In this study, we aimed to assess whole-mount GG in PCa accurately using a novel ML approach to identify appropriate candidates for RP and to compare it with biopsy-proven GG (bxGG).

Materials and Methods

Study Design

A total of 146 patients with histologically-confirmed PCa from the pilot study of a prospective clinical trial (clinicaltrials.gov NCT02659527) were retrospectively enrolled, all of whom underwent ⁶⁸Ga-PSMA-11 PET/MR scans before RP between May 2014 to April 2020 at the Division of Nuclear Medicine in the Vienna General Hospital. This clinical trial complied with the Helsinki Declaration and its amendments. The inclusion and exclusion criteria were listed in **Supplementary Method M1**. The primary aim of this prospective trial was to improve the detection rate of primary localized PCa using non-invasive PSMA PET/MR in comparison with conventional biopsy. Our study, in contrast to previous work, incorporates radiomics, pathomics and genomics data, offering a more comprehensive analysis while predicting whole-mount Gleason grading rather than the improvement of detection rate. The study was approved by the ethics committee of the Vienna General Hospital (ID: 1649/2016). Each subject gave prior written informed consent.

Clinical Data Acquisition

Clinical parameters, including age, weight, height, body mass index (BMI), and pre-operative prostate-specific antigen (PSA) levels in serum were collected from the documentation of the clinical trial.

Based on ⁶⁸Ga-PSMA PET/MR images, two nuclear medicine physicians (S.R. and A.H.) with more than 10 years of experience, blinded to the outcome of each patient, assessed six parameters: (1) lesion involvement: whether the tumor affected one or two lobes or was diffusely spread throughout the prostate; (2) lesion position in the anatomy zone: whether the tumor was located in the central zone (CZ), transition zone (TZ), peripheral zone (PZ), anterior

fibromuscular stroma (AFS), or it was diffusely distributed (i.e., tumor lesions involving at least two anatomical zones or the whole prostate; (3) extracapsular extension: whether the tumor exceeded the prostate capsule; (4) contact with neurovascular bundles: whether the tumor infiltrated adjacent neurovascular bundles; (5) lymph node (LN) infiltration: whether the tumor infiltrated the pelvic or distant LNs; (6) bone metastasis: whether tumor metastasized to bones.

Genomics Data Acquisition

Formalin-fixed paraffin-embedded (FFPE) tissue sections (3×10 μm) were obtained from RP samples and DNA extraction was performed. Genomic libraries were prepared and the raw sequencing data were processed. Somatic small variants were identified from paired samples of the tumor and corresponding normal tissue using the SomaticSeq variant caller [22].

Identified variants were annotated using Ensembl's Variant Effect Predictor (VEP) tool. Pathogenicity scores from the evolutionary model of variant effect (EVE) [23], Combined Annotation-Dependent Depletion (CADD) [24], and PolyPhen [25] were annotated and combined into a final pathogenicity metascore for each identified variant after normalization. Pathogenic genetic disruption was computed as the sum of combined pathogenicity scores of all variants in the given gene. Pathway genetic disruption was subsequently computed as the sum of the pathogenicity scores of all genes in each pathway based on the Kyoto Encyclopedia of Genes and Genomes (KEGG).

The tumor mutational burden (TMB) for each sample was computed as the number of identified somatic variants per million base pairs of the sequence region. Copy number variants (CNVs) were called using the CNVkit tool[26] with the set of paired normal samples used as a panel of "normals" in the computation. CNV burden was computed as the ratio of CNV sum size to the sum size of all sequenced regions. More details are described in

Supplementary Method M2 and Supplementary Figure S1.

Radiomics Data Acquisition

The imaging protocol was described in a previously published study [27]. ⁶⁸Ga-PSMA-11 PET/MR images were acquired and volumes of interest (VOIs) were delineated on PET

images with the T2-weighted imaging (T2WI) as anatomical reference. The delineations were performed manually by two nuclear medicine physicians (S.R and A.H) with more than 10 years of diagnostic experience in a slice-by-slice fashion. In instances of differing viewpoints, the physicians reached a consensus through discussion, ensuring precise and accurate identification of the VOIs. PET image intensities were converted to standardized uptake values (SUV) normalized to body weight, and conventional SUV metrics were extracted from VOIs, including SUV_{min}, SUV_{max}, SUV_{mean}, SUV_{peak}, PSMA-tumor volume (PSMA-TV) and total lesion-PSMA (TL-PSMA) [28].

Radiomics features were computed using PyRadiomics 3.0.1 [29]. All extracted features were compliant with the international biomarker standardization initiative (IBSI) [30]. PET images were resampled to an isotropic voxel size of 2x2x2 mm³ using B-spline interpolation and bin width was set to 0.3 SUV units. The workflow is shown in **Supplementary Figure S2**.

Pathomics Data Acquisition

Tissue samples were obtained from FFPE specimens. Tumor areas and normal areas from each sample were delineated on hematoxylin and eosin (H&E)-stained slides by an uro-pathologist with over 30 years of diagnostic experience (L.K.). Three cylindrical cores (diameter: 2.2 mm) were punched from annotated tumor areas and three from normal areas. These cores were transferred to a recipient paraffin block to create an array of tissue samples. The recipient block was sectioned into 2-5 μm thick sections and TMA slides were prepared. The tumor cores were specifically chosen from areas within the RP specimens that presented the most aggressive features upon pathological morphology in order to be most representative of the PCa tissue aggressiveness.

H&E and IHC staining were performed on the TMA slides. PSMA[31], androgen receptor (AR) [31], Ki-67[32], PSA[31], NK3 homeobox 1 (NKX3.1) [31], cyclin-dependent kinase 2 (CDK2) [33,34], cluster of differentiation 3 (CD3) [35], signal transducer and activator of transcription 3 (STAT3) [36], fatty acid synthase (FASN) [31], thyroid hormone receptor beta (TRβ) [37] and interleukin-6 signal transducer (IL6ST)[38] were selected as targets. The antibodies for IHC

staining were listed in **Supplementary Method M3**.

The uro-pathologist (L.K.), blinded to the clinical data, evaluated the GS of each core based on H&E-stained TMA slides. As the punching process effectively mimics the targeted biopsy in clinical routines[39,40], the GS from each core was considered as bxGS to eliminate any time discrepancy. Moreover, the pathologist determined the percentages of strongly, moderately, or weakly stained cells of each core on IHC slides using the modified H-score [41], which was calculated using the formula: $([\% \text{ of weak staining}] \times 1)$ or $([\% \text{ of moderate staining}] \times 2)$ or $([\% \text{ of strong staining}] \times 3)$, yielding a range from 0 to 300 [42,43]. The average and maximum H-score values from tumor cores were considered representative indicators of different targets' expression levels. The workflow is shown in **Supplementary Figure S3**.

Reference standard

As binary ML prediction target, the post-operative International Society of Urological Pathology (ISUP) grading derived from whole-mount samples was split into low-risk (ISUP < 3) and high-risk (ISUP \geq 3) [44]. This aligns with a previous large multicenter study indicating that the best prognostic stratification can be achieved at the threshold of grade three [45]. The ISUP grading system allows for better interpretation of morphological patterns and more accurate GG stratification [46,47].

Machine Learning

The resulting 203 input features included 13 clinical features, 113 radiomics-wide features (107 radiomics features and 6 conventional SUV metrics), 53 genomics features, 23 pathomics features, and 1 feature, namely biopsy-proven ISUP (bxISUP). All the features are listed in **Supplementary Table S1**.

ML was conducted using five classification algorithms, namely k-nearest neighbors (kNN), random forest (RF), extreme gradient boosting (XGB), support vector machine (SVM) and logistic regression (LGR). Robust performance evaluation was performed using 100-fold stratified Monte Carlo cross-validation with 70% of samples in the training set and 30% in the test set. The test set was exclusively used for testing, while a subset of the training data was

employed for preprocessing and hyperparameter tuning. Features with more than 30% missing values were excluded. Any remaining missing values were imputed using k-nearest neighbor imputation with distance weighting [48]. Features were normalized using z-score. Feature selection was performed using minimum redundancy and maximum relevance (mRMR) [49]. Hyperparameter tuning was performed using random search. All procedures, including imputation, normalization, feature selection, and hyperparameter tuning, were performed separately for each fold while fitting on the training set and performing corresponding transformations on the test set to avoid any data leakage. Probability calibration was performed using an isotonic regression.

To ensure maximum transparency of the ML models and to enable the interpretation of decisions made by the applied algorithms, a set of explainable artificial intelligence (XAI) methods were employed, Shapley additive explanations (SHAP), permutation feature importance, and surrogate models. Permutation and SHAP importance both show feature importance, but the calculation of importance values differs [50]. Surrogate models are post-hoc explainable artificial intelligence techniques that aim to estimate the predictions of black-box models using a simple and interpretable model. In this study, we extracted this description from the RF model to create a simplified diagnostic workflow (decision tree). Further details on ML are described in **Supplementary Method M4**.

Statistical Analysis

The Python 3 package-scipy package 1.11.4 was used for statistical analysis. Quantitative metrics were calculated as mean \pm standard deviation (SD), and categorical variables as percentages. Mann-Whitney test was used for comparison between quantitative variables. The chi-square test was used for comparison between categorical variables. All *p* values were tested as two-tailed. *P* values less than 0.05 were regarded as statistically significant.

Results

Data Overview

A total of 65 PCa patients (age: 64 ± 7.6) with clinical, genomics, radiomics, and pathomics

data were included for final analysis following the cohort flow chart in **Figure 1**. Of these patients, 28 (43%) patients (age: 62.4 ± 7.9) were categorized as low risk (ISUP < 3) and 37 (57%) patients (age: 65.2 ± 7.1) as high risk (ISUP \geq 3). Clinical and imaging parameters of both groups are shown in **Table 1**.

Based on the KEGG database, a total of 10,305 genes were identified in the exome of DNA. The overall mutation frequency was low, with only 29 genes mutated in $\geq 10\%$ of patients (**Supplementary Figure S4**). No significant correlation ($p \geq 0.05$) was found between any of the gene mutations and TMB, CNV burden, or whole-mount ISUP. Due to the sparse distribution of gene mutations, only pathway-level genomics features were employed for the subsequent ML analysis (Figure 2). Among 341 pathways annotated in the KEGG database, 51 pathways were selected due to their association with PCa tumorigenesis, aggressiveness, progression, or metastasis. The literature is listed in **Supplementary Table S2** to show the predictive potential of 51 pathways.

In total, 107 radiomics features were extracted and categorized into shape (n=14), histogram (n=18), and texture (n=75) features. Texture features included 24 gray level co-occurrence matrix (GLCM), 16 gray level run length matrix (GLRLM), 16 gray level size zone matrix (GLSZM), 14 gray level dependence matrix (GLDM) and 5 neighboring gray-tone difference matrix (NGTDM) features. Features are categorized in **Supplementary Table S3**.

ISUP grading was determined by H&E-staining with morphological details depicted in **Figure 3A**. Representative images of PSA expression between ISUP high and low groups are shown in **Figure 3B**. After statistical analysis of the whole cohort, we found that the maximum H-score of PSA was the most distinguished biomarker, and its value in high-risk PCa was lower than that of the low-risk group.

Machine Learning Performance

The five ML models (KNN, RF, SVM, LGR, XGB) were compared based on area under the curve (AUC), accuracy (ACC), sensitivity (SNS), specificity (SPC), positive predictive value (PPV) and negative predictive value (NPV), as depicted in **Figure 4A**. In terms of AUC, the

RF model achieved the highest performance (**Supplementary Table S4**). The AUC, ACC, SNS, SPC, PPV, and NPV of the RF model were 0.87 (95%confidence interval ([CI], 0.85-0.89), 0.78 (95%CI, 0.76-0.80), 0.83 (95%CI, 0.80-0.86), 0.72 (95%CI, 0.68-0.76), 0.79 (95%CI, 0.77-0.81) and 0.80 (95%CI, 0.77-0.83) respectively.

The performance metrics of needle biopsy AUC, ACC, SNS, SPC, PPV, and NPV were 0.75, 0.77, 0.83, 0.61, 0.75, and 0.80 respectively. In comparison, the performance of RF showed an increase in AUC, ACC, SNS, and NPV by 12%, 1%, 11%, and 1%, respectively while SNS and PPV decreased by 6% and 4% (**Figure 4B. 4C**).

A total of 73 features were selected in the validation procedure, consisting of 1 feature, namely bxISUP, 5 clinical features, 12 gene-level genomics features, 43 radiomics-wide features and 13 pathomics features. After comparison of the mean permutation importance of different types of features, bxISUP was identified as the most attributable feature, followed by pathomics, clinical, radiomics, and genomics features (**Figure 4D**). Ranked by permutation importance value, the ten most important features included six radiomics features, three pathomics features, one clinical feature, and biopsy-derived ISUP (**Figure 4E**). More details were described in **Supplementary Results R1-3**.

SHAP importance revealed bxISUP as the most predictive feature, followed by maximum H-score of PSA, and texture/histogram-based radiomics features. **Figure 4F** shows the top 8 features and their SHAP importance values between high and low ISUP groups. In the ISUP high group, ISUP derived from needle biopsy tends to be higher, PSA is less expressed on IHC slides and GLCM Joint Energy values are lower compared to the ISUP low group.

A surrogate model was established to provide a simplified diagnostic workflow describing the more complex ML model (RF). The resulting simplified diagnostic workflow included three features, which were GLCM_Joint Energy, PSAmax_IHC, and bxISUP, which achieved a performance of AUC 0.89 in estimating the output of the complex ML model (**Supplementary Figure S5**). Based on the surrogate model, the ML-based workflow is incorporated in the clinical diagnostic scheme (**Figure 5**). We further performed three analyses, each using a combination of two feature types, including genomics, pathomics, and radiomics as input. AUC

values ranged between 0.84 and 0.89 with the full performance metrics for the individual analyses shown in **Table 2**.

Discussion

In this study, we integrated clinical, imaging, pathomics, and genomics data for the ML-based GG prediction in PCa and demonstrated the superiority of the ML approach over the clinical standard of bxGG assessment. Furthermore, we developed a simplistic and interpretable diagnostic workflow, enabling a software-independent step-by-step procedure for the identification of high-risk patients instead of running the ML software. This makes validation and integration of the presented findings substantially easier since the repeatability and adaptability of ML models are major hurdles for the translation of ML-based software into clinical settings [51,52].

Numerous published multiomics studies in PCa aimed to guide clinical decision-making by directly inferring clinically relevant outcomes and parameters [53–56]. However, most of them focused on predictors from genomics, epigenomics, transcriptomics, and proteomics, omitting image-based predictors, which is problematic given that imaging features have been shown to be important for GS prediction [57–59]. This study addresses this gap by integrating not only PSMA PET radiomics with genomics features but also additional pathomics and clinical features. Thus, by leveraging diverse data sources, the ML model capitalized on comprehensive and complementary underlying information, facilitating more accurate GG assessment.

Despite the slight decrease in SNS and NPV, the AUC, ACC, SPC, and PPV of the ML model were superior to those of needle biopsy. The increased specificity, in comparison with the current clinical standard, indicates that the ML model has the ability to identify low ISUP patients accurately, which is aligned with our goal to avoid unnecessary interventions. Also, the high PPV is indicative of our study's reliability in identifying high-risk patients to provide timely and appropriate treatment.

Despite a discrepancy between bxGG and whole-mount GG, bxISUP was among the most

important features in our analysis. Especially when combining needle biopsy with additional features such as PSA, ML outperformed the current clinical standard of bxGG substantially. Additionally, our findings unveil that PSAm_{ax} as the most important feature in predicting whole-mount GG based on two importance measurement algorithms. PSAm_{ax} represents the maximum H-score of the tumor tissue in needle biopsy and our results denote the more aggressive PCa is, the less PSA the tumor tissue expresses. This is consistent with the study that also explored the correlation between PSA H-scores and GG using TMA slides [60]. In line with other investigations [61], our study identified the first-order radiomics feature Maximum as an important feature in GG prediction. This is because this histogram-based feature, similar to the conventional SUV_{max}, manifests the highest uptake of ⁶⁸Ga-PSMA-11. Of note, our ML model provides a simplified surrogate diagnostic workflow by combining the radiomics feature GLCM_Joint Energy, PSAm_{ax}_IHC, and ISUP in needle biopsy. Following the corresponding decision tree, urologists can select appropriate candidates for RP, which has the potential to revolutionize the diagnostic workflow of PCa. In addition to the two previously mentioned common features, the decision tree also includes GLCM_Joint Energy, a radiomics feature indicative of homogeneous patterns within PCa lesions. The lower Energy value means more heterogeneity within the tumor. Our results demonstrate that PCa with higher GG is more heterogeneous, as previously suggested by a study that identified the transcriptomic heterogeneity of GG 5 groups in a large dataset [62].

Despite the promising results, our study still has several limitations. First, due to its design as a retrospective multiomics study, not all the required parameters were available in some patients, resulting in a relatively small number of subjects for analysis. Second, due to the complexity and unique nature of our study, incorporating an independent validation cohort from another center poses significant challenges, particularly in the retrospective collection of high-dimensional datasets that are consistent with the ones used in our study. However, to ensure the robustness and validity of our findings, employed a rigorous 100-fold Monte Carlo cross-validation scheme, which enhanced the robustness, generalizability, and reduced bias of our study. Third, ML models in medical imaging, specifically in nuclear medicine, are known

to suffer from center-specific variabilities, reducing the reproducibility of radiomics features[63–65]. Consequently, external validation is needed to verify the reliability of the developed approach in the future.

In conclusion, the presented multiomics ML model poses a promising advance in GG assessment for the improved stratification of PCa patients for RP. Our findings have the potential to substantially impact clinical decision-making and personalized management of PCa patients.

Figures and tables

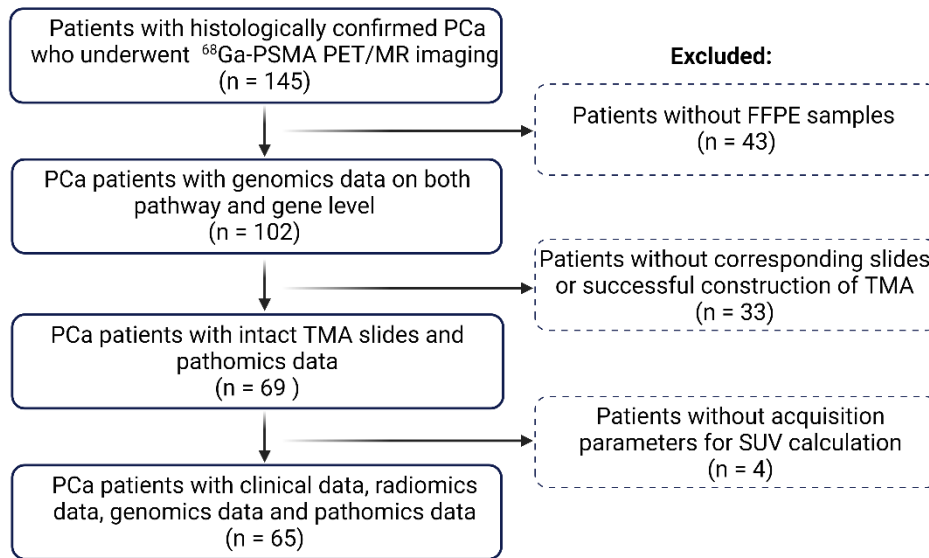


Figure 1: Flowchart of the study cohort. PCa: prostate cancer; TMA: tumor microarray; FFPE: formalin-fixed paraffin-embedded; SUV: standardized uptake value.

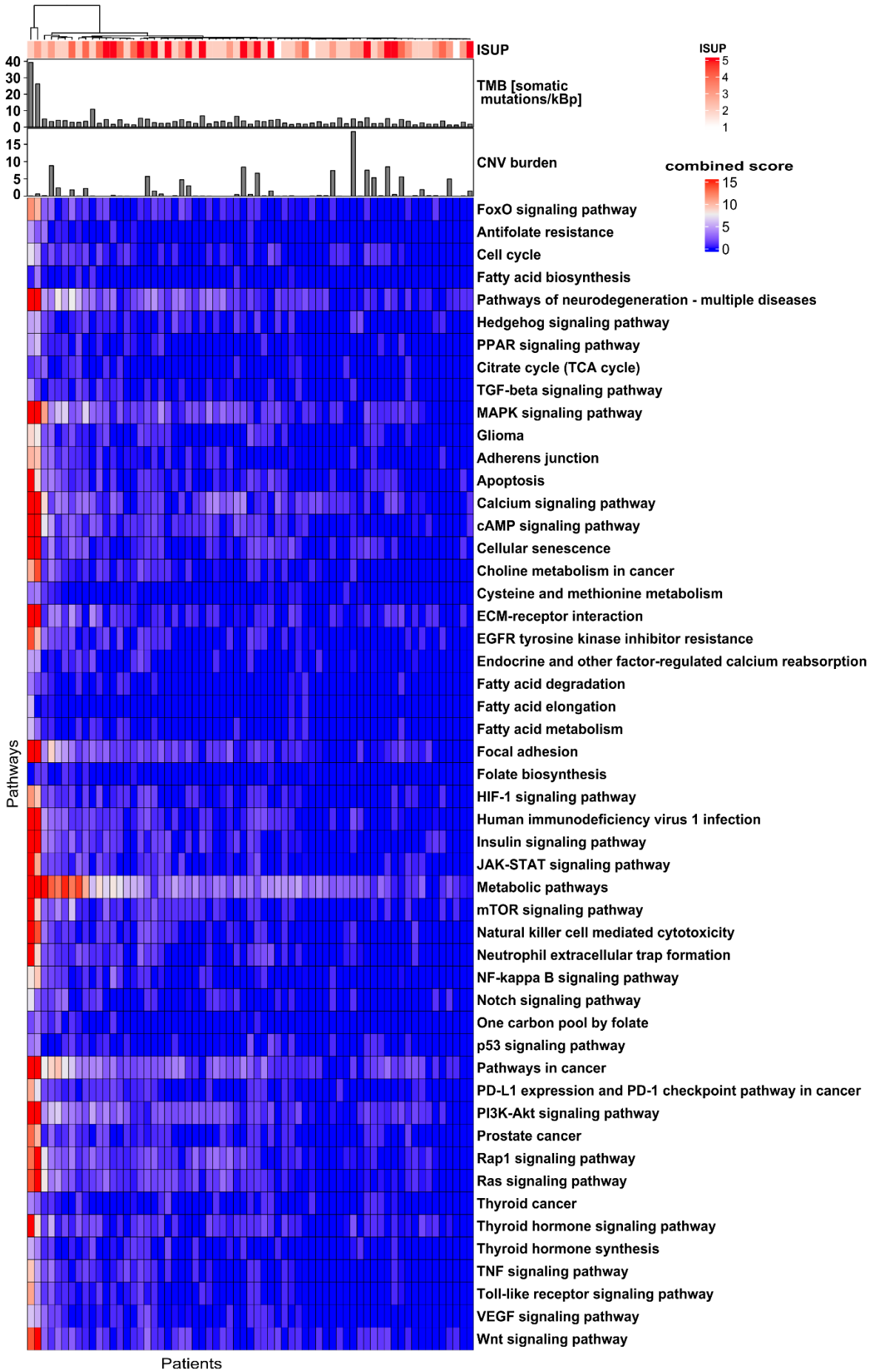


Figure 2: Genomics profile indicates the heterogeneity of the 51 investigated biological pathways in 65 PCa patients. The top bar shows TMB and CNV burden distribution. The top panel shows the correlation of genes/pathways mutation profile with ISUP groups. The top dendrogram shows the clustering patterns of genes/pathways based on their mutation profiles. TMB: tumor mutational burden; CNV: copy number variant; ISUP: International Society of Urological Pathology; PCa: prostate cancer.

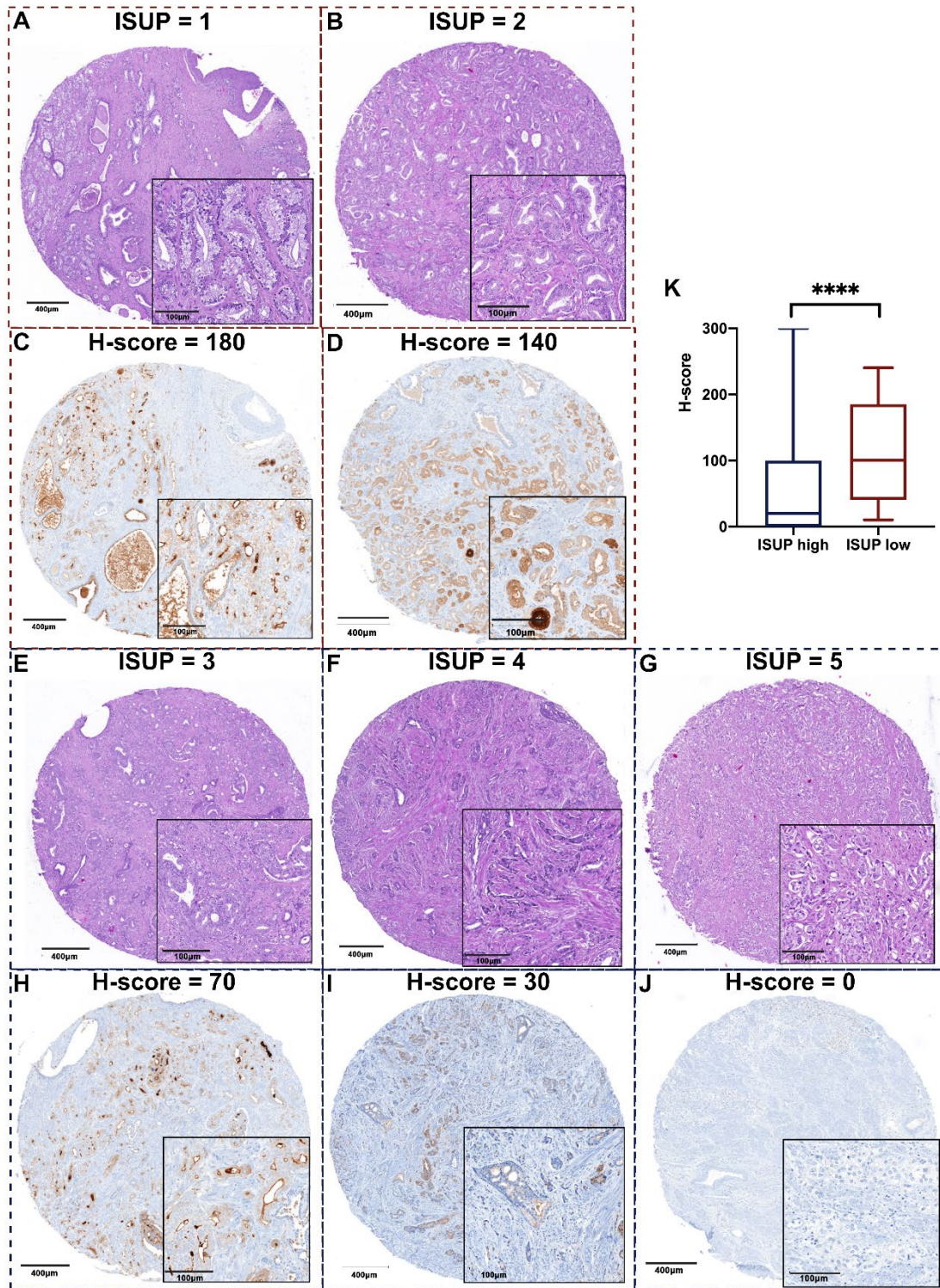


Figure. 3: Representative images of H&E staining and PSA staining on TMA slides revealing less PSA expression when PCa tissue is more aggressive. A. Representative images of H&E staining for each ISUP grade: a. Patient 1, GS 6 (3+3); b. Patient 2, GS 7 (3+4); c. Patient 3, GS 7 (4+3); d. Patient 4, GS 8 (4+4); e. Patient 5, GS 9 (4+5); according

to ISUP consensus 2019. B. Representative images of PSA expression in each ISUP grade core. a. Patient 1, high PSA expression; b. Patient 2, relatively high PSA expression; c. Patient 3, moderate PSA expression; d. Patient 4, relatively low PSA expression; e. Patient 5, negative PSA expression. The corresponding H&E core and PSA core are from the same cylinder of the same patient. The scale bars of the overview core and enlarged details are 400 μm and 100 μm respectively. C. The maximum H-score of PSA is significantly different between ISUP high and low groups ($p < 0.0001$). TMA: tumor microarray; PSA: prostate-specific antigen; ISUP: International Society of Urological Pathology; GS: Gleason score.

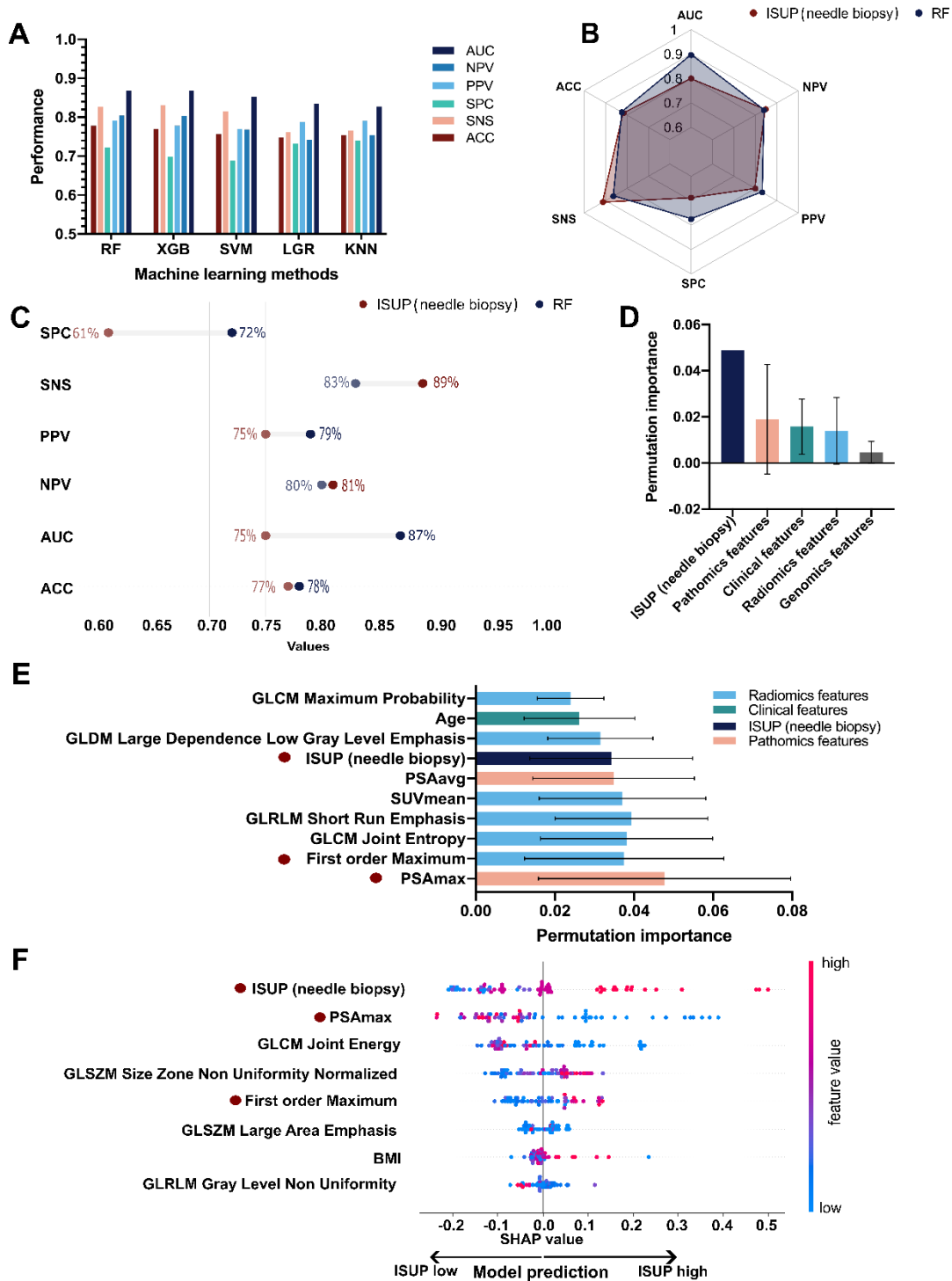


Figure 4. ML Performance of the ISUP prediction in PCa. A. Performance comparison of the five ML algorithms (KNN, RF, SVM, LGR, XGB). Ranked by AUC, the RF model had the best performance. B. Overall comparison of different performance metrics between the RF model and ISUP derived from needle biopsy. C. Comparison of the mean permutation importance between different types of features. D. Detailed comparison of different

performance metrics between the RF model and ISUP derived from needle biopsy. E. The top 10 performing features in ISUP prediction based on permutation importance over all cross-validation folds. F. SHAP importance of the eight features included in the final RF model trained on the entire dataset. Each dot represents a single patient and higher feature values are labeled as red while lower values are blue. The increasing positive SHAP values are indicative of the model's tendency to predict high ISUP while decreasing SHAP values indicate the tendency of the model to predict low ISUP. KNN: k-nearest neighbors; RF: random forest; XGB: extreme gradient boosting; SVM: support vector machine; LGR: logistic regression; AUC: area under the curve; ACC: accuracy; SNS: sensitivity, SPC: specificity; PPV: positive predictive value; NPV: negative predictive value; ML: machine learning; SUVmean: mean standardized uptake value; PSAmax: maximum H-score of PSA expression on three cores of TMA slides; PSAavg: average H-score of PSA expression on three cores of TMA slides.

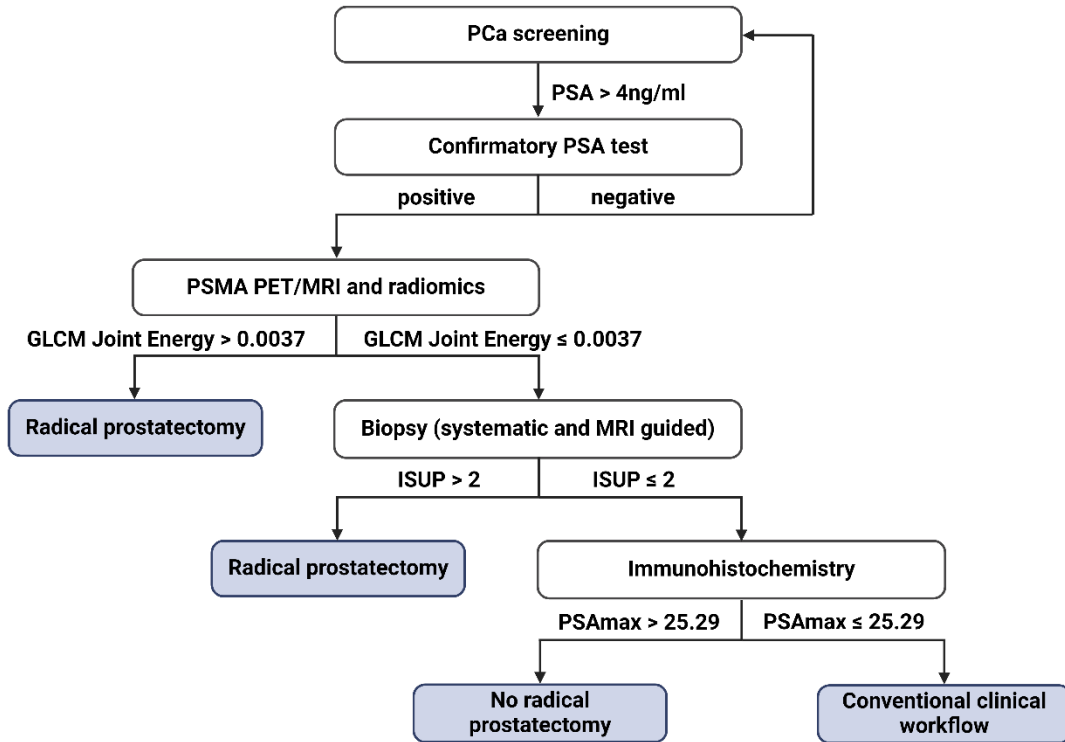


Figure 5: Proposed diagnostic flowchart for prostate cancer (PCa) management.

PSAmax: maximum H-score of PSA expression on three cores of TMA slides; PSA: prostate-specific antigen.

Table 1: Comparison of clinical and imaging parameters between the ISUP low (ISUP<3) group and ISUP high (ISUP≥3) group. Continuous data are expressed as mean ± standard deviation (SD); categorical variables are presented as numbers and percentages.

Parameters		Low risk (ISUP < 3)	High risk (ISUP ≥ 3)	p value
Clinical Parameters				
Age (years)		62.4 (7.9)	65.2 (7.1)	0.14
Weight (kg)		80.5 (10.9)	86.7 (11.1)	0.01
Height (m)		1.8 (0.1)	1.8 (0.1)	0.25
BMI (kg/m ²)		25.8 (2.8)	27.4 (3.3)	0.05
PSA-pre OP (µg/l)		9.4 (8.0)	55.4 (135.0)	<0.001
Pre-OP therapy	No	27 (96.43%)	30 (81.08%)	0.21
	Yes	1 (3.57%)	5 (13.51%)	
	NA	0 (0%)	2 (5.41%)	
Image-based Parameters				
Lesion involvement	<i>One lobe</i>	13 (46.43%)	20 (54.05%)	0.23
	<i>Two lobes</i>	5 (17.86%)	3 (8.11%)	
	<i>Whole prostate</i>	0 (0%)	2 (5.41%)	
	<i>NA</i>	10 (35.71%)	12 (32.43%)	
	<i>NA</i>	10 (35.71%)	12 (32.43%)	
Lesion position in anatomy zone*	<i>CZ</i>	1 (3.57%)	0 (0%)	0.49
	<i>TZ</i>	2 (7.14%)	1 (2.7%)	
	<i>PZ</i>	12 (42.86%)	18 (48.65%)	
	<i>AFS</i>	0 (0%)	1 (2.7%)	
	<i>Diffusion</i>	2 (7.14%)	5 (13.51%)	
	<i>NA</i>	11 (39.29%)	12 (32.43%)	

Extracapsular extension	<i>No</i>	17 (60.71%)	11 (29.73%)	<0.001
	<i>Yes</i>	1 (3.57%)	14 (37.84%)	
	<i>NA</i>	10 (35.71%)	12 (32.43%)	
Contact to neurovascular bundles	<i>No</i>	18 (64.29%)	20 (54.05%)	0.06
	<i>Yes</i>	0 (0%)	5 (13.51%)	
	<i>NA</i>	10 (35.71%)	12 (32.43%)	
Lymph node infiltration	<i>No</i>	17 (60.71%)	17 (45.95%)	0.03
	<i>Yes</i>	1 (3.57%)	9 (24.32%)	
	<i>NA</i>	10 (35.71%)	11 (29.73%)	
Bone metastasis	<i>No</i>	17 (60.71%)	21 (56.76%)	0.38
	<i>Yes</i>	1 (3.57%)	4 (10.81%)	
	<i>NA</i>	10 (35.71%)	12 (32.43%)	
Clinical T staging	<i>cT2a</i>	3 (10.71%)	4 (10.81%)	0.03
	<i>cT2b</i>	5 (17.86%)	2 (5.41%)	
	<i>cT2c</i>	8 (28.57%)	4 (10.81%)	
	<i>cT3a</i>	1 (3.57%)	3 (8.11%)	
	<i>cT3b</i>	1 (3.57%)	12 (32.43%)	
	<i>cT3a+b</i>	0 (0%)	1 (2.7%)	
	<i>cT4</i>	0 (0%)	1 (2.7%)	
	<i>NA</i>	10 (35.71%)	10 (27.03%)	

value in the bracket is standard deviation for numeric data and percentage for categorical data

*CZ: central zone; TZ: transition zone; PZ: peripheral zone; AFS: anterior fibromuscular stroma; Diffusion means PCa lesions involve any two/three anatomy zones or the whole prostate; NA: not applicable.

Table 2: Performance for different input feature type combinations. ACC: accuracy; SNS: sensitivity; SPC: specificity; PPV: Positive predictive value; NPV: Negative predictive value; BACC: Balanced accuracy; AUC: Area under the receiver operating characteristic curve;

Feature types	ACC	SNS	SPC	PPV	NPV	BACC	AUC
Genomics and pathomics	0.805	0.830	0.775	0.822	0.820	0.803	0.893
Radiomics and genomics	0.727	0.743	0.708	0.770	0.716	0.726	0.835
Radiomics and pathomics	0.781	0.820	0.735	0.795	0.803	0.778	0.874
Radiomics, genomics and pathomics	0.779	0.827	0.722	0.791	0.804	0.774	0.869

References:

1. McGuire S. World Cancer Report 2014. Geneva, Switzerland: World Health Organization, International Agency for Research on Cancer, WHO Press, 2015. *Adv Nutr.* 2016; 7: 418–9.
2. Siegel RL, Miller KD, Fuchs HE, Jemal A. Cancer statistics, 2022. *CA Cancer J Clin.* 2022; 72: 7–33.
3. Bill-Axelson A, Holmberg L, Garmo H, et al. Radical Prostatectomy or Watchful Waiting in Prostate Cancer - 29-Year Follow-up. *N Engl J Med.* 2018; 379: 2319–29.
4. Castellan P, Ferretti S, Litterio G, Marchioni M, Schips L. Management of Urinary Incontinence Following Radical Prostatectomy: Challenges and Solutions. *Ther Clin Risk Manag.* 2023; 19: 43–56.
5. Bratu O, Oprea I, Marcu D, et al. Erectile dysfunction post-radical prostatectomy - a challenge for both patient and physician. *J Med Life.* 2017; 10: 13–8.
6. Costello AJ. Considering the role of radical prostatectomy in 21st century prostate cancer care. *Nat Rev Urol.* 2020; 17: 177–88.
7. Mottet N, van den Bergh RCN, Briers E, et al. EAU-EANM-ESTRO-ESUR-SIOG Guidelines on Prostate Cancer-2020 Update. Part 1: Screening, Diagnosis, and Local Treatment with Curative Intent. *Eur Urol.* 2021; 79: 243–62.
8. Yeldir N, Yildiz E, Dündar G. Gleason Score Correlation Between Prostate Needle Biopsy and Radical Prostatectomy Materials. *Turk Patoloji Derg.* 2019; 35: 185–92.
9. Mansouri N, Msakni I, Gargouri F, Khiari R, Bouziani A, Laabidi B. Evaluation of concordance of Gleason score between prostate biopsy and radical prostatectomy. *Tunis Med.* 2018; 96: 430–6.
10. Abedi AR, Basiri A, Shakhssalim N, et al. The Discrepancy between Needle Biopsy and Radical Prostatectomy Gleason Score in Patients with Prostate Cancer. *Urol J.* 2020; 18: 395–9.
11. Li QK, Lih T-SM, Wang Y, et al. Improving the detection of aggressive prostate cancer using immunohistochemical staining of protein marker panels. *Am J Cancer Res.* 2022; 12: 1323–36.

12. Swanson GP, Trevathan S, Hammonds KAP, Speights VO, Hermans MR. Gleason score evolution and the effect on prostate cancer outcomes. *Am J Clin Pathol.* 2021; 155: 711–7.
13. Vollmer RT. Gleason grading, biochemical failure, and prostate cancer–specific death. *Am J Clin Pathol.* 2017; 147: 273–7.
14. Canzler S, Schor J, Busch W, et al. Prospects and challenges of multi-omics data integration in toxicology. *Arch Toxicol.* 2020; 94: 371–88.
15. Loeb S, Ross AE. Genomic testing for localized prostate cancer: where do we go from here? *Curr Opin Urol.* 2017; 27: 495–9.
16. Yip SSF, Aerts HJWL. Applications and limitations of radiomics. *Phys Med Biol.* 2016; 61: R150-66.
17. Norris JM, Simpson BS, Parry MA, et al. Genetic Landscape of Prostate Cancer Conspicuity on Multiparametric Magnetic Resonance Imaging: A Systematic Review and Bioinformatic Analysis. *Eur Urol Open Sci.* 2020; 20: 37–47.
18. Ferro M, de Cobelli O, Vartolomei MD, et al. Prostate Cancer Radiogenomics-From Imaging to Molecular Characterization. *Int J Mol Sci [Internet].* 2021; 22. Available at: <http://dx.doi.org/10.3390/ijms22189971>
19. Gupta R, Kurc T, Sharma A, Almeida JS, Saltz J. The Emergence of Pathomics. *Curr Pathobiol Rep.* 2019; 7: 73–84.
20. Schuettfort VM, Pradere B, Rink M, Comperat E, Shariat SF. Pathomics in urology. *Curr Opin Urol.* 2020; 30: 823–31.
21. McGarry SD, Hurrell SL, Iczkowski KA, et al. Radio-pathomic Maps of Epithelium and Lumen Density Predict the Location of High-Grade Prostate Cancer. *Int J Radiat Oncol Biol Phys.* 2018; 101: 1179–87.
22. Fang LT. SomaticSeq: An Ensemble and Machine Learning Method to Detect Somatic Mutations. In: Boegel S, Ed. *Bioinformatics for Cancer Immunotherapy: Methods and Protocols.* New York, NY: Springer US; 2020: 47–70.
23. Frazer J, Notin P, Dias M, et al. Disease variant prediction with deep generative models of evolutionary data. *Nature.* 2021; 599: 91–5.

24. Rentzsch P, Witten D, Cooper GM, Shendure J, Kircher M. CADD: predicting the deleteriousness of variants throughout the human genome. *Nucleic Acids Res.* 2019; 47: D886–94.
25. Adzhubei I, Jordan DM, Sunyaev SR. Predicting functional effect of human missense mutations using PolyPhen-2. *Curr Protoc Hum Genet.* 2013; Chapter 7: Unit7.20.
26. Talevich E, Shain AH, Botton T, Bastian BC. CNVkit: Genome-Wide Copy Number Detection and Visualization from Targeted DNA Sequencing. *PLoS Comput Biol.* 2016; 12: e1004873.
27. Grubmüller B, Baltzer P, Hartenbach S, et al. PSMA Ligand PET/MRI for Primary Prostate Cancer: Staging Performance and Clinical Impact. *Clin Cancer Res.* 2018; 24: 6300–7.
28. Schmuck S, von Klot CA, Henkenberens C, et al. Initial Experience with Volumetric 68Ga-PSMA I&T PET/CT for Assessment of Whole-Body Tumor Burden as a Quantitative Imaging Biomarker in Patients with Prostate Cancer. *J Nucl Med.* 2017; 58: 1962–8.
29. van Griethuysen JJM, Fedorov A, Parmar C, et al. Computational Radiomics System to Decode the Radiographic Phenotype. *Cancer Res.* 2017; 77: e104–7.
30. Zwanenburg A, Vallières M, Abdalah MA, et al. The Image Biomarker Standardization Initiative: Standardized Quantitative Radiomics for High-Throughput Image-based Phenotyping. *Radiology.* 2020; 295: 328–38.
31. Kristiansen G, Epstein JI. IHC Prostate Pathology [Internet]. [cited July 18, 2023]. Available at: <https://www.patologi.com/DAKO%20immun%20-prostate-pathology.pdf>
32. Maia R, Santos GADOS, Reis S, et al. Can we use Ki67 expression to predict prostate cancer aggressiveness? *Revista do Colégio Brasileiro de Cirurgiões* [Internet]. 2022; 49. Available at: <https://www.scielo.br/j/rcbc/a/pYjPndLW69VXczN94GMrwqk/?format=pdf&lang=en>
33. Zhang J, Gan Y, Li H, et al. Inhibition of the CDK2 and Cyclin A complex leads to autophagic degradation of CDK2 in cancer cells. *Nat Commun.* 2022; 13: 1–16.
34. Yin X, Yu J, Zhou Y, et al. Identification of CDK2 as a novel target in treatment of prostate cancer. *Future Oncol.* 2018; 14: 709–18.

35. Glud EN, Rasmussen M, Zhang Y, et al. Identification of a high-risk immunogenic prostate cancer patient subset as candidates for T-cell engager immunotherapy and the introduction of a novel albumin-fused anti-CD3 × anti-PSMA bispecific design. *Br J Cancer*. 2022; 127: 2186–97.
36. Pencik J, Schleder M, Gruber W, et al. STAT3 regulated ARF expression suppresses prostate cancer metastasis. *Nat Commun*. 2015; 6: 7736.
37. Aksoy O, Pencik J, Hartenbach M, et al. Thyroid and androgen receptor signaling are antagonized by μ -Crystallin in prostate cancer. *Int J Cancer*. 2021; 148: 731–47.
38. Shariat SF, Chromecki TF, Hofer J, et al. Soluble gp130 regulates prostate cancer invasion and progression in an interleukin-6 dependent and independent manner. *J Urol*. 2011; 186: 2107–14.
39. Glinsmann-Gibson B, Wisner L, Stanton M, Larsen B, Rimsza L, Maguire A. Recommendations for Tissue Microarray Construction and Quality Assurance. *Appl Immunohistochem Mol Morphol*. 2020; 28: 325–30.
40. Das CJ, Netaji A, Razik A, Verma S. MRI-Targeted Prostate Biopsy: What Radiologists Should Know. *Korean J Radiol*. 2020; 21: 1087–94.
41. Purdie CA, Quinlan P, Jordan LB, et al. Progesterone receptor expression is an independent prognostic variable in early breast cancer: a population-based study. *Br J Cancer*. 2014; 110: 565–72.
42. Detre S, Saclani Jotti G, Dowsett M. A “quickscore” method for immunohistochemical semiquantitation: validation for oestrogen receptor in breast carcinomas. *J Clin Pathol*. 1995; 48: 876–8.
43. Sowalsky AG, Figueiredo I, Lis RT, et al. Assessment of Androgen Receptor Splice Variant-7 as a Biomarker of Clinical Response in Castration-Sensitive Prostate Cancer. *Clin Cancer Res*. 2022; 28: 3509–25.
44. Epstein JI, Egevad L, Amin MB, et al. The 2014 International Society of Urological Pathology (ISUP) Consensus Conference on Gleason Grading of Prostatic Carcinoma: Definition of Grading Patterns and Proposal for a New Grading System. *Am J Surg Pathol*.

2016; 40: 244–52.

45. Epstein JI, Zelefsky MJ, Sjoberg DD, et al. A Contemporary Prostate Cancer Grading System: A Validated Alternative to the Gleason Score. *Eur Urol*. 2016; 69: 428–35.

46. van Leenders GJLH, van der Kwast TH, Grignon DJ, et al. The 2019 International Society of Urological Pathology (ISUP) Consensus Conference on Grading of Prostatic Carcinoma. *Am J Surg Pathol*. 2020; 44: e87–99.

47. Zelic R, Giunchi F, Fridfeldt J, et al. Prognostic Utility of the Gleason Grading System Revisions and Histopathological Factors Beyond Gleason Grade. *Clin Epidemiol*. 2022; 14: 59–70.

48. Beretta L, Santaniello A. Nearest neighbor imputation algorithms: a critical evaluation. *BMC Med Inform Decis Mak* [Internet]. 2016; 16. Available at: <http://dx.doi.org/10.1186/s12911-016-0318-z>

49. Peng H, Long F, Ding C. Feature selection based on mutual information: criteria of max-dependency, max-relevance, and min-redundancy. *IEEE Trans Pattern Anal Mach Intell*. 2005; 27: 1226–38.

50. Altmann A, Toloşi L, Sander O, Lengauer T. Permutation importance: a corrected feature importance measure. *Bioinformatics*. 2010; 26: 1340–7.

51. Pumplun L, Fecho M, Wahl N, Peters F, Buxmann P. Adoption of Machine Learning Systems for Medical Diagnostics in Clinics: Qualitative Interview Study. *J Med Internet Res*. 2021; 23: e29301.

52. Sandhu S, Lin AL, Brajer N, et al. Integrating a Machine Learning System Into Clinical Workflows: Qualitative Study. *J Med Internet Res*. 2020; 22: e22421.

53. Gómez-Cebrián N, Poveda JL, Pineda-Lucena A, Puchades-Carrasco L. Metabolic Phenotyping in Prostate Cancer Using Multi-Omics Approaches. *Cancers* [Internet]. 2022; 14. Available at: <http://dx.doi.org/10.3390/cancers14030596>

54. Wei Z, Han D, Zhang C, et al. Deep Learning-Based Multi-Omics Integration Robustly Predicts Relapse in Prostate Cancer. *Front Oncol*. 2022; 12: 893424.

55. Wu L, Yang Y, Guo X, et al. An integrative multi-omics analysis to identify candidate DNA

methylation biomarkers related to prostate cancer risk. *Nat Commun.* 2020; 11: 3905.

56. Kiebish MA, Cullen J, Mishra P, et al. Multi-omic serum biomarkers for prognosis of disease progression in prostate cancer. *J Transl Med.* 2020; 18: 10.

57. Abdollahi H, Mofid B, Shiri I, et al. Machine learning-based radiomic models to predict intensity-modulated radiation therapy response, Gleason score and stage in prostate cancer. *Radiol Med.* 2019; 124: 555–67.

58. Chaddad A, Kucharczyk MJ, Niazi T. Multimodal Radiomic Features for the Predicting Gleason Score of Prostate Cancer. *Cancers* [Internet]. 2018; 10. Available at: <http://dx.doi.org/10.3390/cancers10080249>

59. Papp L, Spielvogel CP, Grubmüller B, et al. Supervised machine learning enables non-invasive lesion characterization in primary prostate cancer with [68Ga]Ga-PSMA-11 PET/MRI. *Eur J Nucl Med Mol Imaging.* 2021; 48: 1795–805.

60. Bonk S, Kluth M, Hube-Magg C, et al. Prognostic and diagnostic role of PSA immunohistochemistry: A tissue microarray study on 21,000 normal and cancerous tissues. *Oncotarget.* 2019; 10: 5439–53.

61. Zschaecck S, Andela SB, Amthauer H, et al. Correlation Between Quantitative PSMA PET Parameters and Clinical Risk Factors in Non-Metastatic Primary Prostate Cancer Patients. *Front Oncol.* 2022; 12: 879089.

62. Kishan AU, Romero T, Alshalalfa M, et al. Transcriptomic Heterogeneity of Gleason Grade Group 5 Prostate Cancer. *Eur Urol.* 2020; 78: 327–32.

63. Leithner D, Schöder H, Haug A, et al. Impact of ComBat Harmonization on PET Radiomics-Based Tissue Classification: A Dual-Center PET/MRI and PET/CT Study. *J Nucl Med.* 2022; 63: 1611–6.

64. Da-Ano R, Visvikis D, Hatt M. Harmonization strategies for multicenter radiomics investigations. *Phys Med Biol.* 2020; 65: 24TR02.

65. Orhac F, Frouin F, Nioche C, Ayache N, Buvat I. Validation of A Method to Compensate Multicenter Effects Affecting CT Radiomics. *Radiology.* 2019; 291: 53–9.